

Deletion of microsomal epoxide hydrolase gene leads to increased density in cerebral vasculature and enhances cerebral blood flow in mice

Journal of Cerebral Blood Flow & Metabolism
0(0) 1–15
© The Author(s) 2025
Article reuse guidelines:
sagepub.com/journals-permissions
DOI: 10.1177/0271678X251333234
journals.sagepub.com/home/jcbfm



Anne Marowsky¹, Matthias T Wyss^{1,2}, Diana Kindler³,
Noor-Ul-Ain Khalid¹, Markus Rudin⁴, Bruno Weber^{1,2} and
Michael Arand¹

Abstract

Microsomal epoxide hydrolase (mEH), first identified as detoxifying enzyme, can hydrolyze epoxyeicosatrienoic acids (EETs) to less active diols (DHETs). EETs are potent vasodilatory and pro-angiogenic lipids, also implicated in neurovascular coupling. In mouse brain, mEH is strongly expressed in vascular and perivascular cells in contrast to the related soluble epoxide hydrolase (sEH), predominantly found in astrocytes. While sEH inhibition in stroke has demonstrated neuroprotective effects and increases cerebral blood flow (CBF), data regarding the role of mEH in brain are scarce. Here, we explored the function of mEH in cerebral vasculature by comparing mEH-KO, sEH-KO and WT mice. Basal cerebral volume (CBV₀) was significantly higher in various mEH-KO brain areas compared to WT and sEH-KO. In line, quantification of cerebral vasculature in cortex and thalamus revealed a higher capillary density in mEH-KO, but not in sEH-KO brain. Whisker-stimulated CBF changes were by factor two higher in both mEH-KO and sEH-KO. In acutely isolated cerebral endothelial cells the loss of mEH, but not of sEH, augmented total EET levels and decreased the DHET:EET ratio. Collectively, these data suggest an important function of mEH in the regulation of cerebral vasculature and activity-modulated CBF, presumably by controlling local levels of endothelial-derived EETs.

Keywords

Angiogenesis, cerebral blood flow, EETs, epoxide hydrolase, pericytes

Received 8 July 2024; Revised 3 March 2025; Accepted 22 March 2025

Introduction

Microsomal epoxide hydrolase (mEH) was originally identified as a detoxification enzyme, catalyzing the addition of water to potentially mutagenic epoxides, thus turning them into less active diols.¹ More recent studies indicate that mEH is also capable of hydrolyzing lipid mediators such as epoxyeicosatrienoic acids (EETs) to the respective diols (dihydroxyeicosatrienoic acids, DHETs).^{2–5} EETs are produced from arachidonic acid (AA) by CYP450 epoxygenases in various cell types including neurons, astrocytes and endothelial cells.^{6,7} Four regioisomers are generated by CYP-mediated epoxygenation: 5,6-, 8,9-, 11,12- and 14,15-EETs. In humans and mice, mEH and the soluble epoxide hydrolase (sEH) are the major contributors to EETs hydrolysis and thereby control their levels.⁸ Under non-saturating conditions, when EET levels

are low, mEH and sEH hydrolyze EETs with comparable turnover rate. At higher concentrations of EETs,

¹Institute of Pharmacology and Toxicology, University Zürich, Zürich, Switzerland

²Neuroscience Center Zurich, University and ETH Zurich, Zurich, Switzerland

³Institute of Biomedical Engineering, University Zürich/Eidgenössisch-Technische Hochschule (ETH), Zürich, Switzerland

⁴Loop Zurich, Medical Research Center, Zürich, Switzerland

Corresponding authors:

Anne Marowsky, University of Zurich, Winterthurerstrasse 190, Zurich 8057, Switzerland.

Email: marowsky@pharma.uzh.ch

Michael Arand, University of Zurich, Winterthurerstrasse 190, Zurich 8006, Switzerland.

Email: arand@pharma.uzh.ch

sEH becomes the major enzyme for hydrolysis due to its higher K_M and maximal velocity V_{max} .⁴ Moreover, the two EHs display distinct regioisomeric preferences. mEH prefers the epoxy-moiety on mid-chain olefins, displaying highest enzymatic efficacy (K_{cat}/K_M) for 11,12-EETs > 8,9-EET >> 14,15-EETs. In contrast, sEH turnover is highest for 14,15-EETs with its epoxy group furthest away from the carboxy group, followed by 11,12-EET > 8,9-EET.⁹

In vascular and perivascular mouse brain cells, mEH exhibits particularly strong expression. It is found in high levels in pericytes and endothelial cells, with markedly lower levels in astrocytes. sEH is found exclusively and in high levels in astrocytes.^{2,10}

Overall, EETs are involved in a multitude of physiological and biological functions, specifically in the vasculature. In the cerebral vasculature, EETs are known as strong vasodilators and important mediators in neurovascular coupling, referring to the spatio-temporal coupling of brain activity with local blood flow.^{11–13} Upon activation, neurons release glutamate, which in turn activates calcium influx into astrocytes. This leads to AA release from the membrane by the calcium-activated phospholipase A2, and finally AA epoxygenation to EETs by astrocyte- and endothelium-expressed CYP epoxygenases.^{6,14,15} EETs exert their vasodilatory effect by activating calcium-activated K^+ channel (BKCa) via a $G\alpha_s$ -protein mediated mechanism in smooth muscle cells, leading to K^+ efflux, hyperpolarization and finally vasorelaxation.^{16,17} Increasing EET levels by deletion of the sEH gene or pharmacological inhibition of sEH improves cerebral blood flow (CBF) and reduces infarct size after cerebral ischemia.^{18–21} To our knowledge, only one study has thus far addressed the role of mEH in cerebral vasculature. Substitution of mEH with a more active variant, leading to lower EET and higher DHET levels, is associated with a reduced increase in acetazolamide-triggered cerebral blood volume (CBV) relative to WT mice.²²

EETs are also involved in mitogenesis and neoangiogenesis in various types of vasculature.^{23–25} Regioisomer-specific effects have been observed particularly with angiogenesis, as an early study reported strongest effects with 8,9-EETs in cerebral endothelial cells in an *in vitro* and *in vivo* assay.²⁶ Another study showed that out of the four EET regioisomers only 5,6- and 8,9-EETs were capable of promoting endothelial cell migration and formation of capillary-like structures *in vivo*.²⁷ For revascularization in wound healing, regioisomeric effects appear to be less pronounced. General enhancement of EET levels by sEH deletion accelerates wound healing by promoting endothelial proliferation; application of 11,12- and 14,15-EETs proved similarly effective.^{25,28–30}

Considering the localization of mEH and its capacity to hydrolyze pro-angiogenic and vasodilatory EETs, we hypothesized that mEH may play a significant role in cerebral vascular functions, potentially regulating cerebral vasculature and CBF neurovascular coupling. To test this hypothesis, we first determined basal cerebral blood volume (CBV_0) by susceptibility contrast enhanced magnetic resonance imaging (SCE-MRI) in various brain areas and compared it across all three genotypes (mEH-KO, sEH-KO, WT littermates as controls). Next, we visualized and quantified the vasculature, using immunohistochemistry (IHC) in brain slices. To delineate the particular contribution of each EH to cerebrovascular dynamics, whisker pad-stimulated hemodynamic changes in the barrel cortex were recorded by laser speckle imaging. Finally, as EHs exert their effects via controlling EETs, we determined their levels in acutely isolated cerebral endothelial cells and compared those to cortex homogenate to identify local EH effects.

Material and methods

Animals

For the present study male mEH-KO³¹ and sEH-KO³² mice as well as their respective WT littermates were used, aged eight to sixteen weeks. KO mice had previously been backcrossed to a C57BL/6 background for more than ten generations to minimize the influence of confounding factors other than EHs. As no difference between sEH and mEH WT littermates was found, data sets were combined and referred to as WT. All mice were housed in single-ventilated cages. Animals were kept at a standard 12:12 hr dark:light cycle and had ad libitum access to water and standard chow. All procedures were approved by the local veterinary authorities (Veterinaeramt, Kanton Zuerich) according to the guidelines of the Swiss Animal Protection Law (Animal Welfare Act of 16 December 2005, and Animal Protection Ordinance of 23 April 2008). License numbers were ZH004/2015 and ZH188/2012. Experiments have been reported in compliance with the ARRIVE guidelines.³³

Genotyping

Genotypes were assessed by standard polymerase chain reaction (PCR) reaction, using specific primer pairs. Genomic DNA was extracted from mouse ear biopsies and the following primers were used to distinguish between homozygous WT and KO mice: mKO forward 5'-CCC GGG ACA AGG AGG AGA CC-3' and mKO reverse 5'-AAG GAT CAC AGG GTG AAA GGA A-3'. The PCR produced a WT-specific band

at 800 bp and a mEH-KO-specific band at 1400 bp. sKO forward 5'-GCG AGG GGC GGT GCT GAG ATT GG-3', sKO reverse 1 5'-CTG GAA AGC AAT TTG AAA CCT GGG-3' and sKO reverse 2 5'-AGG GTC GCT CGG TGT TCG AGG-3'. Amplification with sKO forward and sKO reverse primers resulted in product sizes of 305 bp for the WT allele, and 1444 bp and 411 bp for the KO allele using the reverse primers sKO reverse 1 and sKO reverse 2, respectively.

CBV₀ recordings by susceptibility contrast-enhanced MRI (SCE-MRI)

Experiments were performed on a Pharmascan MR system 47/16 (Bruker BioSpin, Germany) operating at a magnetic field strength of 4.7T. Mice were anesthetized with an initial dose of 3% isoflurane, endotracheally intubated and actively ventilated at a rate of 90 breaths per minute. For SCE-MRI recordings, the isoflurane level was reduced to 1% and the head was fixed in a stereotaxic device. A dose of 21 mg/kg of the neuromuscular blocking agent gallamine (Sigma Aldrich) was administered i.v. For assessing CBV₀ values, a multi spin echo Rapid Acquisition with Relaxation Enhancement (RARE) sequence sensitive to changes in the transverse relaxation rate was used with the following acquisition parameters: repetition time TR: 3333.33 ms, echo time TE: 8.12 ms, RARE factor: 32, field-of-view FOV: 2.00 cm × 1.34 cm, matrix dimension MD: 133 × 100 pixels, coronal slice thickness SLTH: 1.00 mm, interslice distance ISD: 1.5 mm, number of slices N_{slices}: 8, number of averages NA: 4. This resulted in a axial volume coverage of 11.5 mm with a temporal resolution of 40 s/volume. Regions of interest (ROIs) were delineated on the relevant image slice using the Franklin and Paxinos mouse atlas. With regard to the cortex, somatosensory and motor cortex areas were analyzed. Eight sequential volumes were recorded for determining the baseline intensity S_{pre}, followed by bolus injection of the superparamagnetic ironoxide nanoparticles Endorem® (Guerbet SA, Roissy, France) at a dose of 60 mg Fe/kg. After 20 min, 30 sequential image volumes were recorded for assessing the post-contrast intensity S_{post}.

Image analysis: MRI data were analyzed as previously described.³⁴ In brief, administration of the contrast agent led to an increase of the transverse relaxation rate $R_{2,CA}(\infty) = R_{20} + r_{2,CA} \cdot c_{CA}(\infty) \cdot CBV_0$, with R_{20} and $R_{2,CA}(\infty)$ denoting the transverse relaxation rates prior and after contrast agent administration, $r_{2,CA}$ the molar relaxivity of the contrast agent, $c_{CA}(\infty)$ its concentration, and CBV_0 the baseline cerebral blood volume. The infinity symbol indicates that the concentration of the contrast agent has reached a quasi steady-state. It is assumed that administration of the contrast

agent does not affect CBV₀. The baseline cerebral blood volume can then be calculated for selected brain regions of interest from the relative signal attenuation according to

$$CBV_0 = -\frac{1}{r_{2,CA} \cdot c_{CA}(\infty) \cdot TE} \cdot \ln\left(\frac{S_{post}}{S_{pre}}\right)$$

with S_{pre} and S_{post} representing the signal intensity prior and after contrast agent administration.

Immunofluorescence staining

Mice were injected with pentobarbital (i.p., 50 mg/kg) and subjected to transcardiac perfusion with standard Ringer's solution. Brains were rapidly extracted and postfixed for three hrs at 4°C in 4% paraformaldehyde, cryoprotected in 30% sucrose/PBS and sectioned with a microtome to 40 µm-thick coronal slices. Slices (6 per animal) were evenly spaced every 600 µm, with the first slice positioned at the bregma, the last one at Bregma -3.00 mm. The following antibodies were used: anti-CD13 (goat, R&D Systems, #AF2335, 1:500), anti-CD31 (rat, Novus Biologicals, #NB600-1475, 1:100), anti-GFAP (chicken, Abcam, ab4674 (1:2000), anti-mEH (rabbit, in-house, 1:10'000), anti-mEH (goat, Detroit R&D, #MEH1, 1:1000), anti-sEH (rabbit, in-house, 1:2000), anti-fibrinogen (clone JG37-18, MA534, Life technologies; 1:3000). For IHC, sections were incubated overnight at 4°C with first antibodies in appropriate dilutions in Tris-saline buffer, containing 2% normal serum and 0.2% Triton-100. After rinsing they were incubated with secondary antibodies conjugated to either Alexa 488 (Molecular Probes, 1:400), Cy3 or Cy5 (Jackson ImmunoResearch Laboratories, 1:400), diluted in Tris-buffer containing 2% normal serum for 60 min at room temperature. Finally, slices were mounted on gelatin-coated object slides using mounting medium with DAPI (Sigma, #F6057). For IHC staining of acutely isolated (peri)vascular cells, cells were spread on a gelatin-coated object slide and allowed to dry. Antibody staining procedures including antibodies used were similar to the one executed with slices.

Image acquisition and processing

High-magnification images were acquired by laser scanning confocal microscopy (Zeiss LSM 700 and 800), using a 25× Plan-Apochromat lens (numerical aperture of 1.4) and ZEN software. For the vasculature analysis 20 to 22 µm thick z-stacks (spaced by 1.5 µm) of confocal layers were taken in predefined areas in cortex and thalamus. Images measured 1024 × 1024 pixels with pixels scaled to 0.5 µm × 0.5 µm. Per mouse, six sections with a total of 36 cortical and 36

thalamic ROIs ($512\ \mu\text{m} \times 512\ \mu\text{m} \times 20\ \mu\text{m}$) were analyzed. ROIs were placed as shown in Figure 2(c). The person taking, preprocessing and analyzing the images was blind to the genotype. Images were preprocessed using the open-source software FIJI for converting z-stacks to 2D images, using the function maximum intensity z-projection. For the analysis of area coverage in %, total vessel length and number of branch points (bifurcation density) a previously published Matlab script³⁵ was used, allowing to batch-process all images with the same parameters. Overlap of immunoreactivity was calculated using ZEN blue software edition 2.6.

Determination of basal 20-HETE levels in mouse brain homogenate (cortex)

Mice were anesthetized with isoflurane (2.5% in air/oxygen 70%/30%), decapitated and brains were rapidly removed. The cortex was dissected and snap-frozen in liquid nitrogen. To 50-100 mg homogenized cortex tissue 250 μL methanol/acetonitrile (1:1) including 3 μL deuterated internal standard (d6-20-HETE, 1 ng/ μL , Adipogen Switzerland) were added. Samples were incubated for 30 min at -80°C , sonified for 10 min and pelleted for 5 min at 13,000 rpm (4°C). The supernatant was diluted with 4.5 mL H_2O and directly before SPE extraction formic acid was added to a final concentration of 0.1%. Supernatants were applied to ISOLUTE[®] C18 solid phase extraction columns (Biotage, Uppsala, Sweden), preconditioned with 1 mL acetonitrile and subsequently with 1 mL PBS/5% methanol. Columns were washed twice with 1 mL PBS buffer containing 5% methanol and evaporated to dryness. Lipids were eluted with $3 \times 600\ \mu\text{L}$ ethylacetate in tubes containing 10 μL trapping solution (30% glycerol in methanol), dried under nitrogen, dissolved in 100 μL methanol/20 mM Tris (pH 7.4) (1:1) and analysed by LC-MS/MS (see *Materials and Methods/MS quantification of EET/DHET levels from endothelial/astrocytic cells*).

RNA extraction and assessment of gene expression (eNOS) from cortical tissue

RNA was isolated from 25 mg samples of frozen cortical tissue, using the RNeasy Mini Kit (Qiagen #74104) including RNase-free DNase (Qiagen #79254) treatment. The RNA concentration was measured with a UV-Vis spectrometer (NanoDrop ND-1000, Witec AG, Switzerland). For each sample, 500 ng RNA were reverse-transcribed with a cDNA reverse transcription kit (Thermo Scientific #K1612). Gene expression was quantified by real time PCR (EvaGreen[®]qPCR Mix Plus, #08-25-0000S, Lucerna-Chem) on a 7900 HT Fast Real-time PCR system

(Applied Biosystems). Data analysis was carried out applying the comparative Ct method with *Gapdh* used to normalize the amounts of cDNA in each sample.

Primer sequences for eNOS: 5'- AGG ACC CCC GGC GCT ACG AAG AA-3' and 5'-GTG GGC GCT GGG TGC TGA ACT GA-3'. For GAPDH: 5'-CCT GCT TCA CCA CCT TCT TGA-3' and 5'-CAT GGC CTT CCG TGT TCC-3'.

Preparation of cytosolic and microsomal fractions from cortical tissue, assessment of 20-HETE generation and functional turnover assays with 8,9-, 11,12- and 14,15-EETs

Preparation and assays were performed as described in detail earlier including the LC-MS/MS settings.³ Turnover assays with 8,9-EETs were carried out in presence of 10 μM trans-4-[4-(3-Adamantan-1-yl-ureido)-cyclohexyloxy]-benzoic acid (tAUCB, a gift from Christophe Morisseau, UC Davis) if indicated. For assessment of the 20-HETE production rate in microsomal fractions, 5 μM AA were added.

Extraction and isolation of endothelial/astrocytic cells

Mice were anesthetized with isoflurane (2.5% in air/oxygen 70%/30%), decapitated and brains were rapidly removed and transferred into 2 mL PBS, pH 7.4, containing 0.5% BSA, 0.5 mg DNase and 0.5 mg papain. Brains were cut into small pieces and incubated for 30 min at 37°C . To stop the papain reaction DMEM with 10% FBS was added. Cells were pelleted by centrifugation at $300 \times g$, washed with PBS containing 0.5% BSA (PBS/BSA) and pipetted up and down with a Pasteur pipet to yield a single cell suspension. The cell suspension was filtered (30 μm filter, MyltenyiBiotec #130-041-407) and then subjected to myelin removal using the MiltenyiBiotec magnet system with myelin removal beads (Miltenyi Biotec, #130-096-733, LS-column #130-042-401), followed by enrichment of CD31-positive cells by using CD31 microbeads (MiltenyiBiotec, #130-097-418). For elution of CD31-enriched cells, the column was removed from the magnet and 5 mL PBS/BSA were added. Cells were counted, centrifuged and re-suspended in 150 μL DMEM/10%FBS and incubated for 1 hr at 37°C and 5% CO_2 .

MS quantification of EET/DHET levels from endothelial/astrocytic cells

150 μL acetonitrile:methanol (1:1), 3 μL internal standards (d11-modified 8,9-,11,12-, 14,15-EETs and -DHETs, 1 ng/ μL for each regioisomer, Adipogen

Switzerland) and 700 μL PBS (pH 7.4) were added to the 150 μL of CD31-enriched cell suspension in DMEM/10%FBS. After centrifugation the supernatant was applied to ISOLUTE[®] C18 solid phase extraction columns (Biotage, Uppsala, Sweden), primed with $2 \times 1 \text{ mL}$ acetonitrile and $2 \times 1 \text{ mL}$ PBS (pH 7.4)/5% methanol (1:1). The columns were washed with 1 mL PBS (pH 7.4)/5% methanol (1:1), dried, and eluted with $3 \times 600 \mu\text{L}$ ethylacetate. After drying under nitrogen, samples were re-suspended in 100 μL methanol/20 mM Tris (pH 7.4) (1:1) and subjected to LC-MS/MS analysis. For the detailed method including all quantifier transitions, see literature.³ In brief: Analytes were separated on a Gemini C18 NX column ($2 \times 150 \text{ mm}$, 5 μm pore size, Phenomenex Helvetia GmbH, Basel) and a pre-column using an Agilent 1100 liquid chromatography system. The mobile phase consisted of eluent A (water containing 0.0125% ammonia) and eluent B (acetonitrile with 0.0125% ammonia). It was injected at a flow rate of 350 $\mu\text{L}/\text{min}$ with a volume of 40 μL . Compounds were eluted using a linear gradient from 16 to 26% of eluent B for 2 min, followed by a linear gradient from 26 to 36% of eluent B within 16 min and from 36 to 95% within 0.7 min. An isocratic flow of 95% B was held for 1.6 min and finally the column was re-equilibrated for 4.2 min with 16% B. The HPLC system was coupled to a QTRAP 4000 quadrupole ion trap mass spectrometer (AB Sciex, Framingham, MA, USA) equipped with an electrospray interface. Analytes were assessed in negative mode. Quantification of samples was done by determining the area under the peak using Multiquant software. Values were corrected for extraction efficiency using the internal standard peak area.

Intrinsic optical imaging

Surgery. For surgical procedures animals were anesthetized with isoflurane (2.5% in air/oxygen 70%/30%). The skull above the somatosensory cortex was carefully thinned to translucency using a dental drill and the area was then covered with low melting point agarose (1% in Ringer's solution) and sealed with a circular glass coverslip of 4-mm diameter. The animals' temperature was kept at 37°C with a heating blanket. After surgery, the animal was transferred to the imaging setup, isoflurane was discontinued and anesthesia was maintained with ketamine/xylazine (90 mg/10 mg per kg bodyweight i.p.).

Optical imaging and stimulation. 20 min after induction of ketamine/xylazine anesthesia, imaging was performed. Following a baseline of 4 s, the whisker pad contralateral to the imaged hemisphere was stimulated using

subcutaneous electrodes with 16-pulse trains (400 μA , 4 Hz, 4 s, 1 ms pulse length) generated by a stimulus generator (Multichannel Systems STG).

Cortical images were acquired using a 12-bit CCD camera attached to a motorized Leica MZ16FA epifluorescence stereomicroscope using dynamic laser speckle imaging. The method is described in detail elsewhere.³⁶ In short, a 785-nm laser light was shone onto the cortex and images were acquired at 30 Hz with an exposure time of 10 ms. Each acquisition consisted of 10 trials separated by a 30 s intertrial interval and for each animal one to two acquisitions were performed.

Data Analysis. Image analysis was performed using custom-written Matlab routines and the software package PMOD (PMOD Technologies, Zürich, Switzerland). The ten trials of one acquisition were averaged. The magnitude of functional intrinsic signals was calculated as the fractional change in reflected light intensity relative to prestimulus baseline ($\Delta I/I_0\%$). To quantify CBF, speckle images were processed using 5×5 spatial and 25 temporal binning (for further details see literature³⁶) Circular regions-of-interest (1 mm^2) were drawn manually over the area of maximal signal increase to extract the signal time course.

Injection of Evans Blue dye for blood brain barrier integrity

Blood brain barrier integrity was tested as described before.³⁷ In short, 50 μL Evans's blue (Sigma-Aldrich, #E2129) in 0.9% NaCl (2%, 2 mL/kg) were injected into the mouse tail vein. After four hrs mice were transcardially perfused with standard Ringer's solution containing 2 mM calcium. Brains were rapidly removed and snap-frozen in liquid nitrogen. The next day one hemisphere was homogenated in 1 mL trichloroacetic acid (50%) and centrifuged for 30 min at 12'000 rpm at 4°C. 240 μL of the supernatant were mixed with 720 μL ethanol and fluorescence intensity was measured at 620/680 nm at a Tecan M200 Pro against a standard curve.

Statistics

Data are displayed as mean \pm SD, unless otherwise stated. Data sets were subjected to normality tests and, if normality was confirmed, to 1-way and 2-way ANOVAs, followed by suitable posthoc tests including Tukey's, Sidak's and Fisher's LSD test. Respective posthoc tests are indicated in the legends. If normality was not confirmed, the median was calculated and an appropriate non-parametric test (Man-Whitney-U-test)

performed. SPSS software and GraphPad Prism9 were used for all statistical calculations.

Results

mEH is extensively expressed in cerebral endothelial cells, pericytes and astrocytes

To confirm mEH transcriptome data¹⁰ in vascular and perivascular cells on protein level, we performed IHC stainings in WT mouse brain slices, using specific antibodies for EHs,² astrocytes (marker: GFAP), endothelial cells (marker: CD31) and pericytes (marker: CD13). CD13-positive cells around larger vessels (diameter >10 μm) were assumed to be smooth muscle cells, known from an earlier study to be mEH-positive.² mEH-immunoreactivity (IR) co-localized almost completely with CD13-IR around capillaries and larger vessels, and less with CD31- and GFAP-IR

(Figure 1(a) to (e), inset, Table 1). This corresponds with the RNA expression profile, which shows strongest expression of mEH in pericytes, followed by expression in smooth muscle and endothelial cells (see Supplementary data, Figure 1(a)¹⁰). sEH-IR was largely confined to astrocytes (Figure 1(f)) in line with the transcriptome data (Supplementary data, Figure

Table 1. Co-localization of EH IR with (peri)vascular markers.

Marker	Number of analyzed images (n)	Overlap of IR (%) ^a
mEH with CD13	9	87.2 ± 10.9
mEH with CD31	9	68.7 ± 9.4
mEH with GFAP	9	55.7 ± 9.7
sEH with CD31	8	0.8 ± 1.2
sEH with GFAP	8	52.4 ± 14.8

^aMean ± standard deviation.

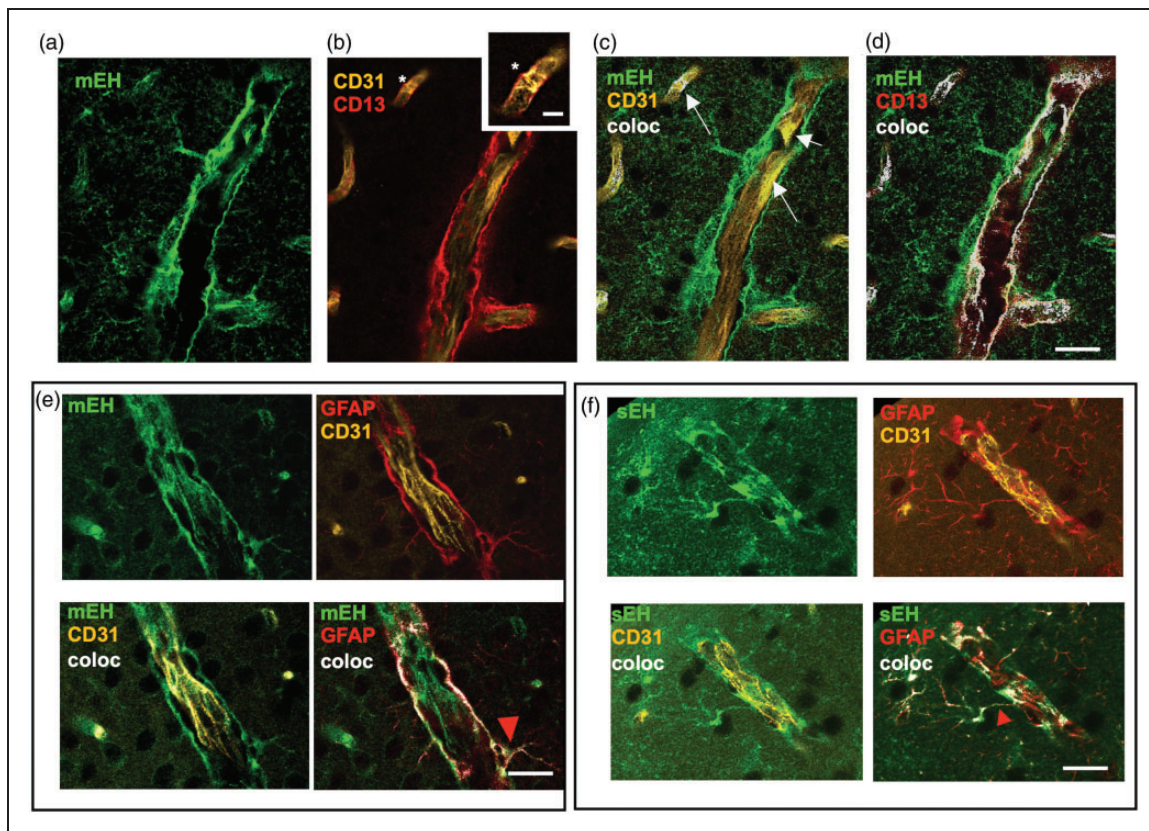


Figure 1. IHC stainings in WT cerebral vasculature with EH antibodies and (peri)vascular markers. (a) mEH-positive structures comprise both vascular and perivascular structures. Image taken in the cortical area. (b) Co-labeling of endothelial cells with CD31 (yellow) and mural cells with CD13 (red). Mural cells include pericytes around capillaries (marked with an asterisk, see enlarged in the inset) and smooth muscle cells around larger vessels. (c) Co-labeling of mEH (green) with CD31 (yellow) reveals partial co-localization, indicated by white arrows. (d) Co-labeling of mEH (green) with CD13 (red) reveals substantial co-localization of mEH with CD13. (e) mEH and GFAP co-localize in subsets of astrocytes with mEH present in astrocytic endfeet (red arrowhead indicates astrocytic endfoot). Image taken in cortical area and (f) Co-labeling of GFAP with sEH confirms sEH expression in astrocytes, here shown in the cortex. Note the sEH-positive astrocytic endfoot on the vessel (red arrowhead). sEH and CD31 do not overlap. Scale bars (a)–(f) 20 μm, inset: 5 μm.

1(b), Table 1). Since we intended to use mEH- and sEH-KO mice in CBV_0 and CBF experiments, KO brain slices were stained with EH antibodies to determine potential compensatory changes in the cellular localization of the remaining EH. The same cell types as in WT were positive in KO mice (see Supplementary data, Figures 2 and 3), thus cell-type specific expression of the remaining EH was preserved in both KO mice strains.

Deletion of mEH leads to an increase in CBV_0

To gain initial insights into the role of mEH in the cerebral vasculature, we recorded CBV_0 , using SCE-MRI. MRI allows probing the entire brain, including deeper brain structures such as hippocampus, striatum and thalamus, however with limited resolution (voxel dimensions: $150\ \mu\text{m} \times 130\ \mu\text{m} \times 1000\ \mu\text{m}$). In all five brain areas measured (cerebellum, cortex, striatum, hippocampus, thalamus) mice lacking mEH showed

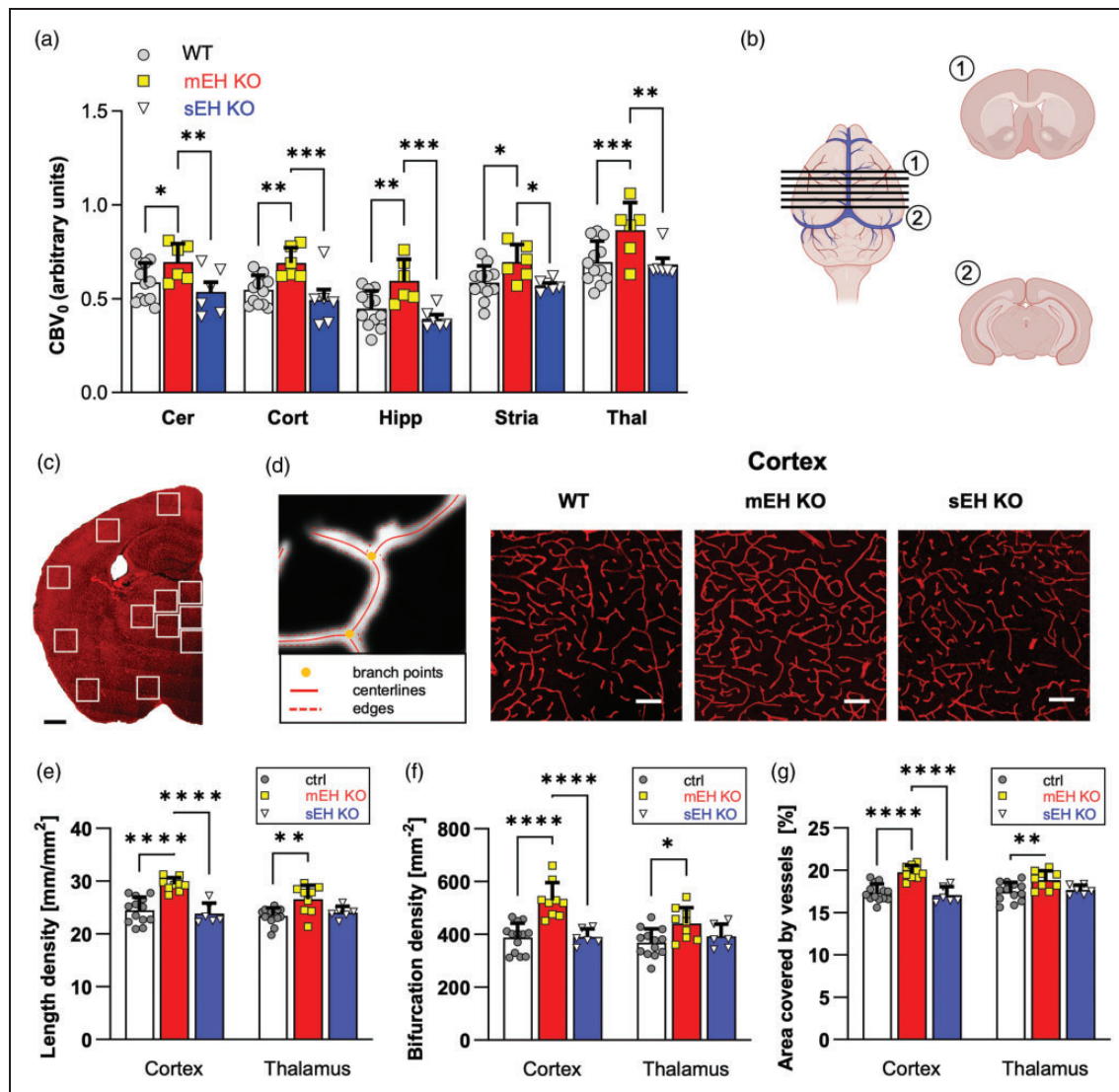


Figure 2. Comparison of CBV_0 and quantification of vascular density in WT, mEH KO and sEH KO mice. (a) CBV_0 was measured in the cerebellum (Cer), cortex (Cor), hippocampus (Hipp), striatum (Stria), and thalamus (Thal) across all genotypes by SCE-MRI. WT $n = 12$, mEH KO $n = 6$, sEH KO $n = 6$ animals. 2-way ANOVA followed by Fisher's LSD test. (b) Schematic for two-dimensional image analysis, showing the position of the six sections with the first (1) positioned at the Bregma and the last (2) positioned at Bregma $-3\ \text{mm}$. (c) Coronal section of a WT brain with CD31 staining and areas sampled for quantification shown in white. (d) Example of a binarized image processed by batch-applied automated analysis and representative images of corresponding cortical areas in WT, mEH KO and sEH KO brains. (e–g) Quantification of total vessel length, bifurcation density and area covered by vessels stratified for cortex and thalamus. WT $n = 13$, mEH KO $n = 9$, sEH KO $n = 6$ animals. 2-way ANOVA followed by Tukey's posthoc test. * $p < 0.05$, ** $p < 0.01$, *** $p < 0.001$, **** $p < 0.0001$. Only statistically significant comparisons are shown. All values are mean \pm SD. Scale bars (c) 1 mm; (d) 20 μm .

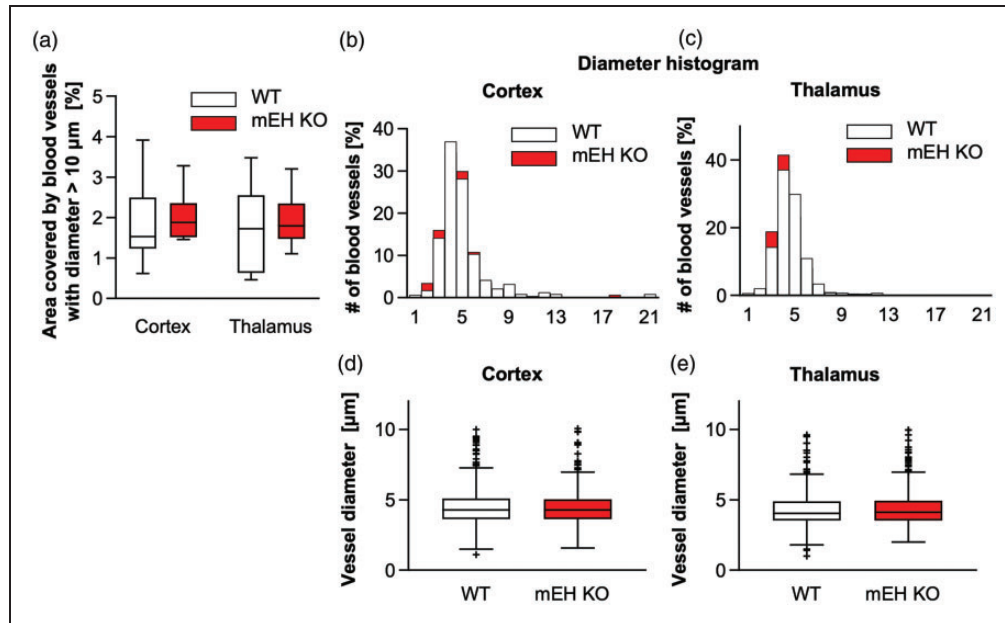


Figure 3. Vessel caliber distribution and vessel diameters of WT and mEH KO blood vessels in cortex and thalamus. (a) Comparison of area covered by blood vessels with diameter $>10\ \mu\text{m}$ in cortex and thalamus. WT $n=9$, mEH KO $n=9$ animals. Man-Whitney U test, performed for each brain area separately, revealed no significant genotype-specific difference. Cortex $p=0.605$, thalamus $p=0.546$. (b) and (c) Frequency distribution of vessel calibers for the two brain areas in WT and mEH KO brains. (d) and (e) Comparison of median diameters of microvessels $<10\ \mu\text{m}$. Unpaired t test with Welch's correction revealed no genotype-specific difference. Cortex $p=0.380$, thalamus $p=0.844$. Number of vessels analyzed in cortex: WT $n=591$, mEH KO $n=583$; thalamus: WT $n=1220$, mEH KO $n=1274$.

significantly higher CBV_0 values compared to WT. In contrast, CBV_0 values in sEH-KO brains were comparable to those of WT animals (Figure 2(a)). The higher CBV_0 values observed in mEH-KO brain could either be caused by a) an increase in vascular density (resulting from enhanced angiogenesis or decreased vascular pruning), b) by a more dilated vasculature, or c) by a combination of a) and b).

Capillary density is higher in mEH-KO mice

To assess the cerebral vasculature in mEH-KO, sEH-KO, and WT mice, brain slices were stained with the CD31 antibody. We focused on two brain areas, cerebral cortex and thalamus, as they are well-defined brain regions and represent one area with strong sEH-expression (cortex) and one with weaker sEH-expression (thalamus).² In each section six ROIs were placed across the cerebral cortex to capture values representative of different regions. Whenever possible, ROIs were placed to span all layers from the pial surface to the gray matter-white matter interface to account for layer-specific variations in capillary density.³⁸ Additionally, six ROIs per section were placed in the thalamus (Figure 2(b) and (c)). These predefined areas were imaged across genotypes and quantified for the parameters total length, bifurcation density,

and total area covered by vessels (Figure 2(d) to (g)). Comparison between genotypes revealed a significant increase in all parameters in mEH-KO relative to sEH-KO and WT brains. Specifically, mEH-KO showed statistically significant increases of 15% for area coverage by vessels and for total vessel length, and an increase of 30% in bifurcation density for both brain areas. In contrast, WT and sEH-KO mice did not differ significantly in any parameter, suggesting that mEH, but not sEH, plays a role in modulation of cerebral network density.

Next, we addressed whether increases in vessel diameter contributed to CBV_0 changes in mEH-KO mice. Analysis of vessel area coverage data revealed that only $\sim 2\%$ of all analyzed vessels fall into the macrovasculature category (diameter $>10\ \mu\text{m}$) with the majority ($\sim 98\%$) classified as microvasculature or capillaries. The area covered by macrovessels did not differ between mEH-KO and WT for cortical and thalamic areas (Figure 3(a)), indicating that differences in vascular density are attributable exclusively to capillaries. The formation of large penetrating vessels occurs during embryonic stages, whereas capillarization primarily takes place postnatally.³⁹ This aligns with the ontogenetic expression of Ephx1 in mouse brain, which rises substantially after birth.⁴⁰ Since capillary diameters are not normally distributed, we calculated and compared the respective medians. Median diameters

were similar in mEH-KO and WT mice (Figure 3(d) and (e)), suggesting that lack of mEH does most likely not cause pre-dilated capillaries under basal conditions (Cortex: WT 4.273 μm vs mEH-KO 4.272 μm , Thalamus: WT: 4.032 μm vs mEH-KO: 4.123 μm). The distribution of the vascular diameter in both examined areas is similar between mEH-KO and WT (Figure 3(b) and (c)) and is consistent with previous studies of cerebral microvasculature diameters in mice.^{41,42}

Higher rCBF values in both EH-KO compared to WT mice

To assess the contribution of each EH to neurovascular coupling, we used electrical whisker pad stimulation and monitored changes in relative CBF (rCBF) in the somatosensory cortex with laser speckle imaging

(Figure 4(a)). Stimulation-induced changes in rCBF were significantly higher in mEH- and sEH-KO compared to WT mice, reflected by the higher area under the curve (AUC, Figure 4(b) and (c)) and the higher amplitude (Figure 4(d)). In all genotypes, there was no difference in the onset and the peak time of the blood flow response. The substantially increased CBF response in both KO strains suggests that ambient EET levels are elevated due to the absence of one of the EHs, and that the residual EH is unable to completely compensate for this condition.

EET levels are changed in mEH-KO, but not in sEH-KO endothelial/astrocytic cells

Given the pivotal role of EETs as “effector” molecules in the neurovascular response and in angiogenesis, we

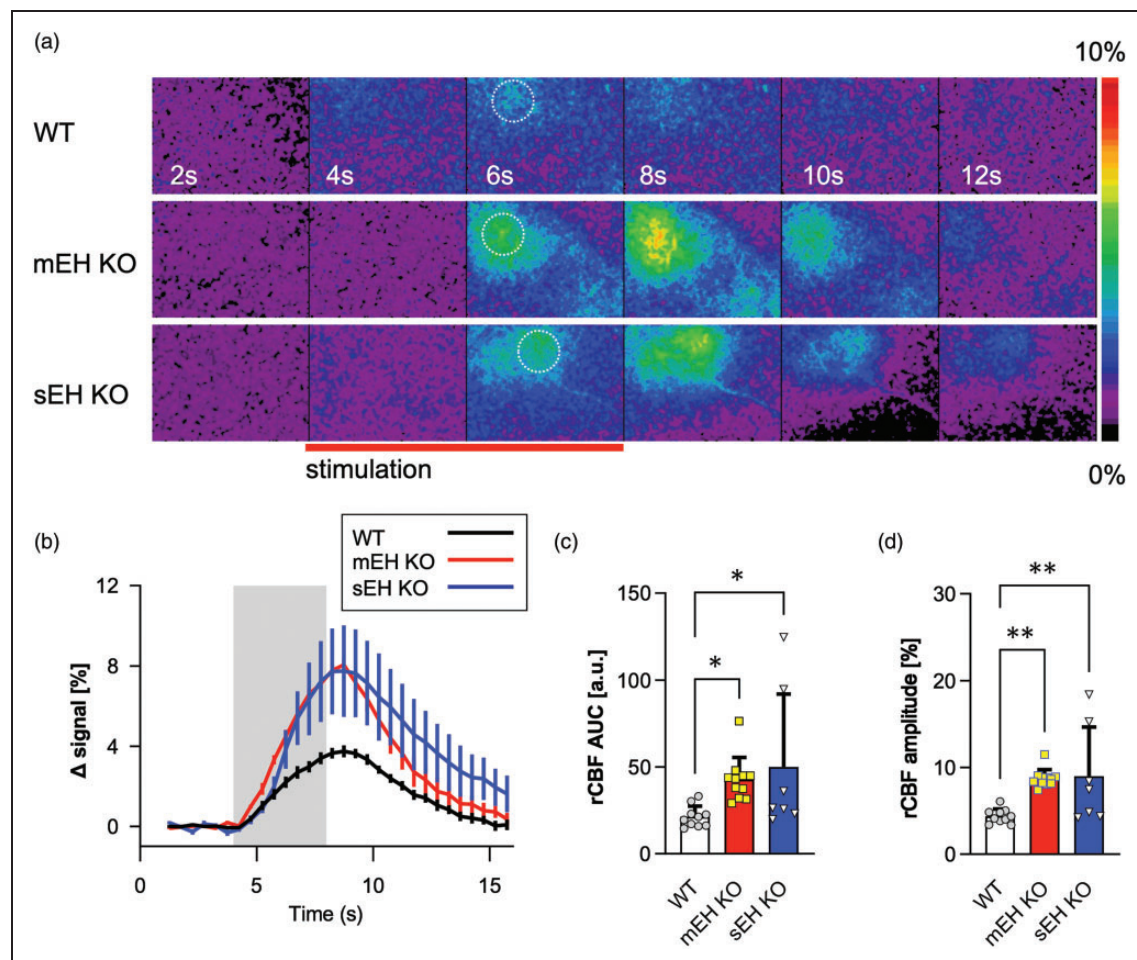


Figure 4. rCBF recordings in WT, mEH and sEH KO somatosensory cortex. (a) Heat maps, showing representative time-dependent changes in rCBF for each genotype; whisker-pad stimulation is indicated by the red line below. Circles at the 6-second time point indicate the region-of-interest (ROI), which was analyzed. (b) Stimulation, carried out for four seconds as indicated by the grey column, led to a rapid increase in rCBF in the somatosensory cortex. Shown are averaged traces for each genotype \pm SEM. (c) and (d) Quantifications of area under the curve (AUC) and change in rCBF amplitude. WT $n = 10$ acquisitions from 6 animals, mEH KO $n = 11$ from 6 animals, sEH KO $n = 7$ from 6 animals. 1-way ANOVA followed by Tukey's post hoc test. Data in (c) and (d) are presented as mean \pm SEM. * $p < 0.05$, ** $p < 0.01$.

finally quantified EETs and DHETs in acutely isolated cerebral endothelial cells to assess the impact of mEH on local EET levels. Cells were isolated using CD31-coated beads and their identity was assessed by FACS (data not shown) and confirmed by fluorescence

immunostaining with respective antibodies. 91% of the isolated cells were identified as endothelial cells, the remaining cells as astrocytes (~8%) and single pericytes (~1%; Figure 5(a)), hence termed endothelial/astrocytic cells from here on. Lack of mEH led to

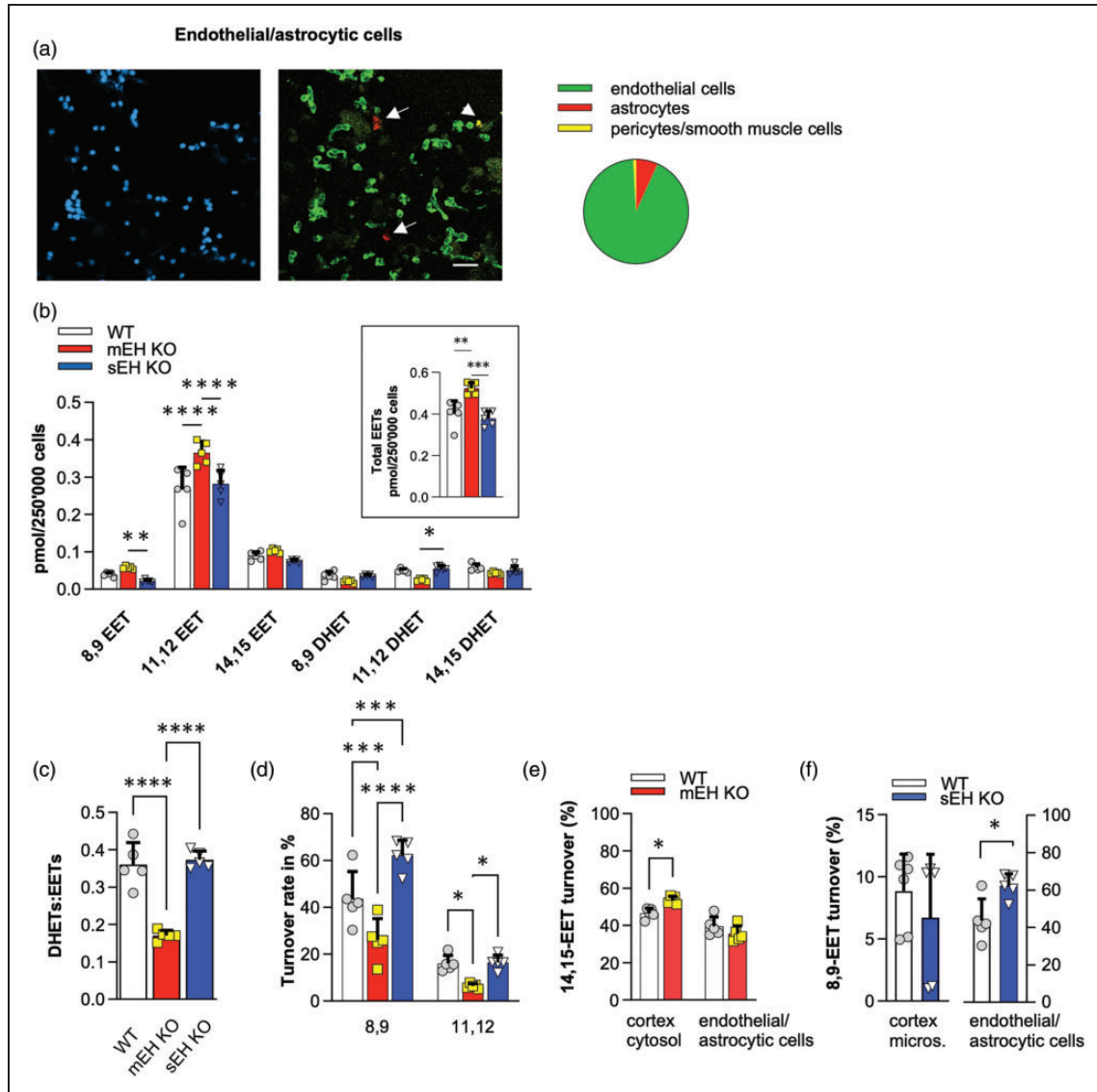


Figure 5. EET-DHET profile in acutely isolated endothelial/astrocytic cells from KO and WT brains. (a) Representative image of acutely isolated vascular and perivascular cells from total brain, labelled with DAPI (left) and with CD31 (green, endothelial cells), GFAP (red, astrocytes) and CD13 (yellow, mural cells) (right). White arrows point to astrocytes, the white arrowhead to a mural cell. Distribution of cell types relative to total DAPI count is summarized to the right (pie chart). (b) EET-DHET profile with regioisomers in endothelial/astrocytic cells. $n = 5$ animals for all genotypes. 2-way ANOVA, Tukey's post-hoc test. Legend also applies to b) inset. Inlay: Total amounts of EETs (sum of 8,9-, 11,12- and 14,15-EETs). 1-way ANOVA, followed by Sidak's post-hoc test. (c) DHET:EET ratio. 1-way ANOVA, Tukey's post hoc test. (d) Turnover rates for 8,9- and 11,12-EETs. 2-way ANOVA, Fisher's LSD test. $n = 5$ for all genotypes. (e) Turnover assay with 14,15-EETs to assess compensatory sEH upregulation in mEH KO cortex and endothelial/astrocytic cells, suggesting sEH upregulation in total cortex tissue but not in isolated endothelial/astrocytic cells. 2-way ANOVA, Sidak's posthoc test and (f) Turnover assay with 8,9-EETs in WT and sEH KO cortex microsomes and endothelial/astrocytic cells in presence of the sEH inhibitor tAUCB ($10 \mu\text{M}$), indicating mEH upregulation in endothelial/astrocytic cells, which is not detectable in total cortex tissue. 2-way ANOVA, Sidak's posthoc test. $n = 6$ for both cytosolic and microsomal samples, perivascular cells: $n = 5$ for all genotypes. All values are shown as mean \pm SD. * $p < 0.05$, ** $p < 0.01$, *** $p < 0.001$, **** $p < 0.0001$. Scale bar a) $20 \mu\text{m}$.

higher EET and a lower DHET:EET ratio compared to WT and sEH-KO, in accordance with dominant mEH expression in endothelial cells (Figure 5(b) plus inset, 5(c)). DHETs were still detected in mEH-KO endothelial/astrocytic cells (Figure 5(b)), most likely generated by sEH, expressed in astrocytes. Turnover rates were particularly high for 8,9-EET (Figure 5(d)).

The loss of either mEH or sEH is often compensated by upregulation of the remaining EH as observed in the liver.³ Functional turnover assays with 14,15-EETs as substrate for sEH and 8,9-EETs for mEH revealed that sEH upregulation in mEH-KO cortex homogenate does occur, as 14,15-EET turnover was higher in mEH-KO cytosolic fraction compared to WT. However, in the isolated cells containing primarily mEH-expressing endothelial cells, we found no indication for upregulation consistent with the low percentage of sEH-expressing astrocytes (Figure 5(e)). The opposite was the case in sEH-KO samples. Here, mEH upregulation indicated by higher 8,9-EET turnover, was only observed in isolated endothelial/astrocytic cells, but not detectable in whole cortex samples (Figure 5(f)). This suggests that mEH effects are mainly local. Compensatory upregulation may also include other vasoactive mediators such as the vasoconstrictory and pro-angiogenic 20-HETE (20-hydroxyecosatetraenoic acid) and the vasodilatory and pro-angiogenic autacoid nitric oxide (NO). Renal 20-HETE levels were

reportedly increased in sEH-KO male mice compared to WT.⁴³ In acutely isolated endothelial/astrocytic cells 20-HETE levels were below the detection limit, consistent with the overall low expression level of the major 20-HETE synthases CYP4A and CYP4F in these cells.¹⁰ Analysis of KO and WT cortical brain samples showed significantly decreased ambient 20-HETE levels in mEH-KO (Figure 6(a)) and a reduced capacity to generate 20-HETE in mEH-KO microsomes (Figure 6(b)). Lower 20-HETE levels may contribute to an increase in rCBF in mEH-KO brains. There was no difference in 20-HETE levels between sEH-KO and WT samples (Figure 6(a) and (b)). EETs are known to transcriptionally upregulate the NO-generating enzyme endothelial NO-synthase (eNOS).⁴⁴ To explore potential alterations in the eNOS level, real-time PCR was conducted. mRNA quantitation revealed no difference between genotypes, indicating that eNOS expression is not enhanced in EH-KO brains (Figure 6(c)). However, this does not rule out the possibility that the NO activity is altered by an alternative mechanism in KO brains. Given the expression of sEH in astrocytes, mEH in endothelial cells, pericytes and astrocytes, EHs might be implicated in formation and/or maintenance of the blood-brain barrier (BBB). There was no difference in Evans Blue dye extravasation in KO and WT brains (Figure 6(d)), nor in fibrinogen stainings of all three genotypes (Supplementary data, Figure 4). While

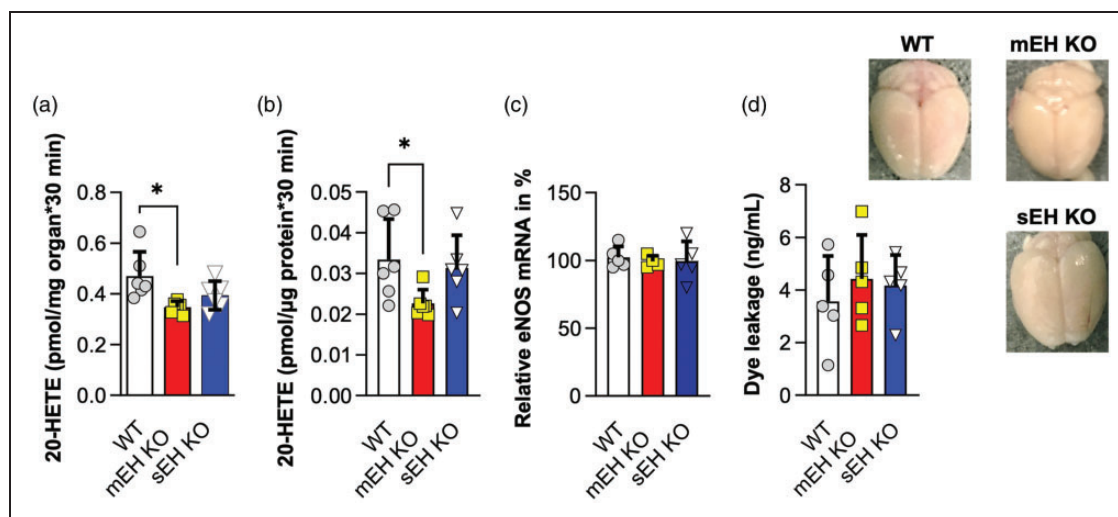


Figure 6. 20-HETE and eNOS mRNA levels and functional test of the blood brain barrier in WT, mEH KO and sEH KO brains. (a) Comparison of ambient 20-HETE levels in cortex homogenates shows lower levels for mEH KO. WT $n = 5$, mEH KO $n = 6$, sEH KO $n = 6$ animals. 1-way ANOVA, Sidak's post-hoc test. (b) Capacity of cortical microsomes to produce 20-HETE in presence of additional AA ($5 \mu\text{M}$) is reduced in mEH KO. $n = 6$ for all genotypes. 1-way ANOVA, Fisher's LSD test. (c) Comparison of relative eNOS mRNA levels revealed no significant alterations between genotypes. 1-way ANOVA, Sidak's post hoc test. $n = 5$ for all genotypes and (d) To test the integrity of the blood-brain barrier, Evan's blue dye was injected into the tail vein and extravasation into brain tissue assessed. Brains of all genotypes remained unstained. Levels of dye leakage in brain homogenate were comparable, indicating that the blood brain barrier was intact in KO brains. 1-way ANOVA, Sidak's post-hoc test. $n = 5$ for all genotypes. All values are shown as mean \pm SD. * $p < 0.05$.

Evan's blue dye shows only major leakage in BBB, fibrinogen stainings are considered more sensitive. Both tests confirmed an intact blood brain barrier in both KO strains.

Discussion

In this study, we demonstrate that: a) mEH is widely expressed in cerebral vascular and perivascular cells, including endothelial cells and pericytes; b) mEH-KO mice show higher CBV_0 values compared to sEH-KO and WT mice in various brain regions, which corresponds with increased capillary density in the thalamus and cerebral cortex of mEH-KO mice; c) mEH is involved in neurovascular coupling; and d) the effects of mEH on the vasculature are likely due to its local regulation of endothelium-derived EETs.

This study highlights distinct roles for mEH and sEH in the cerebral vasculature. Notably, mEH appears to play a unique and exclusive role in promoting cerebral capillarisation, whereas both mEH and sEH are involved in neurovascular coupling. However, the specific role of mEH in shaping capillary density contrasts with earlier findings on sEH, which has been linked to angiogenesis under different conditions. Several studies have shown that sEH inhibitors can improve wound healing, increase neoangiogenesis, and promote tumor growth.^{28,45} These findings, however, were observed under pathological conditions, whereas our experiments (CBV_0 and CBF measurements, as well as vasculature analysis) were conducted in healthy adult mice. In healthy tissue, the role of sEH may be more constrained because cell boundaries are intact, making the cell-specific expression of mEH and sEH particularly important. Moreover, under pathological conditions, other pro-angiogenic compounds are generated such as cyclooxygenase 2 (COX-2). COX2 is upregulated during inflammation and involved in catalyzing the formation of an 8,9-EET derivative, which exerts angiogenic effects with an efficiency similar to that of VEGF.^{46,47}

With regard to angiogenesis, pericyte-endothelial cell signaling is crucial for endothelial cell proliferation, differentiation and stabilization.⁴⁸ Both cell types express exclusively mEH. Pericytes, in particular, are essential for stabilizing microvessels by suppressing capillary regression and promoting endothelial growth.⁴⁹ In the absence of mEH, the increased release of EETs from endothelial cells may facilitate pericyte proliferation and coverage, which in turn helps stabilize endothelial cells. EETs are generally thought to act in a paracrine and autologous manner⁵⁰ and may therefore also have a direct, growth-promoting effect on endothelial cells.

Two key factors may explain why sEH contributes to neurovascular coupling and increased CBF, but not to angiogenesis: (a) the specific expression of EHs in different cell types, and (b) differences in the substrate affinity and saturation levels between mEH and sEH. Upon sensory input, capillaries are estimated to account for 84% of the increase in blood flow, with pericytes controlling their dilation.⁴¹ During functional hyperemia, endothelial cells primarily produce EETs, which then act on peri-capillary pericytes to mediate vasodilation.⁵¹ If EET concentrations are sufficiently high, the mEH located in pericytes and endothelial cells rapidly becomes saturated due to its lower K_M and activity relative to sEH.^{2,9} As a result, endothelial cells will release EETs instead of DHETs. sEH, found in astrocytic processes (Figure 1(f)), will then control the ambient EET concentration. Therefore, both enzymes may play a role in controlling EET levels during functional hyperemia. However, it is important to highlight that in mEH-KO brains, other factors may contribute to the increases in rCBF. Specifically, these include a denser microvascular network and lower levels of the vasoconstrictive compound 20-HETE.

The molecular mechanisms through which EETs induce their angiogenic effects are still not fully understood. Several studies report an upregulation of VEGF and partly CD31^{29,30,52} suggesting an indirect rather than a direct mechanism. Furthermore, specifically 8,9-EETs are capable of triggering NO production in endothelial cells⁵³ with NO promoting cerebral capillary angiogenesis.⁵⁴ Common cellular pathways activated by EETs in angiogenesis include the p38 MAP kinase,²⁷ MEK, ERK and phosphoinositide 3-kinase (PI 3-K) pathway.⁵⁵ Thus far, a specific high-affinity EET-receptor mediating vascular EET effects in brain has not been identified. Such a receptor would be most likely a cell-surface G(s)-coupled receptor, as activation of protein kinase A (PKA) is important for the angiogenic effect.⁵⁶ EET-responsive low-affinity receptors include the endothelial expressed GPR 40⁵⁷ and several subtypes of prostaglandin receptors,⁵⁸ however, none of these receptors appears to be associated with angiogenic effects.

Given that EETs are strong vasodilators, the elevated CBV_0 values in mEH-KO brains could stem from either a more dilated vasculature or a combination of dilation and increased vascular density. We did not find evidence for a more dilated vasculature in mEH-KO brains, since the mean diameter for thalamic and cortical capillaries were similar between mEH-KO and WT brains (Thalamus: WT 4.03 μm , mEH-KO 4.12 μm , Cortex: WT 4.27 μm , mEH-KO 4.27 μm). They compared favorably to microvessel parameters in recent studies, which reported values in the range from $4.2 \pm 0.4 \mu\text{m}$ ⁵⁹ to $6.3 \pm 1.1 \mu\text{m}$ ⁶⁰ in *in vivo* and

from 3.5 to 4 μm in *ex vivo* studies^{38,59,61} We cannot rule out, however, that IHC stainings are less precise in visualizing the outline of vessels than methods used in these studies (fluorescent gel or ink gel), thus more subtle genotype-specific differences might have been overlooked. It should also be noted that we anesthetized with pentobarbital, a barbiturate that exerts well-known vasodilatory effects.⁶²

There are several limitations to this study that should be mentioned. While the CBV_0 recordings were performed in five brain areas (cerebellum, cortex, hippocampus, striatum and thalamus), the analysis of vascular density was limited to two brain areas, cortex and thalamus. Furthermore, we used only male mice, as we anticipated a more pronounced genotype-specific difference in this group. sEH is a sexually dimorphic enzyme with significantly lower expression in the female mouse brain compared to the male.⁶³ Consequently, under ischemic conditions, CBF increases comparably in female WT and sEH-KO mice, while it is almost 50% lower in male WT mice compared to their sEH-KO counterparts.⁶³ A similar pattern of CBF changes was observed in healthy female WT and sEH-KO mice when using sensory input (see Supplementary data, Figure 5).

Furthermore, we used constitutive KO mice, which usually prompts compensatory regulation of several genes and their products, including the one of the remaining EH.³ The increased turnover rates of sEH in mEH-KO brain homogenates and mEH in sEH-KO endothelial/astrocytic cells support this, along with the reduced 20-HETE levels observed in mEH-KO brain. Other vasodynamic players such as the NO-generating enzyme eNOS were not changed on a transcriptional level in the KO strains, yet non-transcriptional changes of NO may possibly still occur. More importantly, EET generation may change as consequence of alteration in CYP expression. In mEH and sEH-KO liver, various CYP epoxygenase isoforms were induced or repressed, leading in sEH-KO to a net reduction of hepatic EETs.³ This makes it likely, that expression of cerebral CYP epoxygenases such as CYP2J6 is changed in KO strains. Epoxygenase activity can be determined by calculating the total of [EETs + DHETs]. There was no statistically significant difference between genotypes, but mEH-KO brains exhibited a slight trend toward higher EET levels (WT: 0.545 ± 0.089 pmol/250'000 cells vs mEH-KO: 0.614 ± 0.132 pmol/250'000 cells vs sEH-KO: 0.523 ± 0.098 pmol/250'000 cells, 1-way ANOVA, Sidak's post-hoc test, $p = 0.0574$). To define the role of mEH in cerebral angiogenesis in more detail and rule out compensatory effects that arise due to the constitutive knock-out, it would be advisable to use selective

mEH inhibitors or inducible knock-out mice in future studies.^{64,65}

In summary, these results illustrate a significant role of mEH in cerebral capillarisation and neurovascular coupling through the regulation of vascular and perivascular EET levels. This role is primarily evident under healthy conditions, but it may change under pathological circumstances, where alterations in cellular boundaries and EET levels could increase the involvement of sEH.

Funding

The author(s) received no financial support for the research, authorship, and/or publication of this article.

Acknowledgements

The authors are grateful to Imke Meyer and Louis Scheurer for expert technical assistance.

Declaration of conflicting interests

The author(s) declared no potential conflicts of interest with respect to the research, authorship, and/or publication of this article.

Authors' contributions

A.M.: concept and design, acquisition, analysis and interpretation of data, drafting of the manuscript; M.T.W.: acquisition, analysis and interpretation of data; D.K.: acquisition and analysis of data; N.U.A.K.: acquisition of data; M.R.: interpretation of data; B.W.: interpretation of data; M.A.: acquisition, analysis and interpretation of data; all co-authors have contributed to the review of the manuscript and approved the final version.

Supplementary material

Supplemental material for this article is available online.

ORCID iD

Michael Arand  <https://orcid.org/0000-0003-2413-3177>

References

1. Oesch F. Significance of various enzymes in the control of reactive metabolites. *Arch Toxicol* 1987; 60: 174–178.
2. Marowsky A, Burgener J, Falck JR, et al. Distribution of soluble and microsomal epoxide hydrolase in the mouse brain and its contribution to cerebral epoxyeicosatrienoic acid metabolism. *Neuroscience* 2009; 163: 646–661.
3. Marowsky A, Meyer I, Erismann-Ebner K, et al. Beyond detoxification: a role for mouse mEH in the hepatic metabolism of endogenous lipids. *Arch Toxicol* 2017; 91: 3571–3585.
4. Edin ML and Zeldin DC. Regulation of cardiovascular biology by microsomal epoxide hydrolase. *Toxicol Res* 2021; 37: 285–292.

5. Morisseau C, Kodani SD, Kamita SG, et al. Relative importance of soluble and microsomal epoxide hydrolases for the hydrolysis of epoxy-fatty acids in human tissues. *Int J Mol Sci* 2021; 22: 4993.
6. Alkayed NJ, Narayanan J, Gebremedhin D, et al. Molecular characterization of an arachidonic acid epoxigenase in rat brain astrocytes. *Stroke* 1996; 27: 971–979.
7. Carver KA, Lourim D, Tryba AK, et al. Rhythmic expression of cytochrome P450 epoxigenases CYP4 × 1 and CYP2c11 in the rat brain and vasculature. *Am J Physiol Cell Physiol* 2014; 307: C989–998.
8. Morisseau C, Inceoglu B, Schmelzer K, et al. Naturally occurring monoepoxides of eicosapentaenoic acid and docosahexaenoic acid are bioactive antihyperalgesic lipids. *J Lipid Res* 2010; 51: 3481–3490.
9. Decker M, Adamska M, Cronin A, et al. EH3 (ABHD9): the first member of a new epoxide hydrolase family with high activity for fatty acid epoxides. *J Lipid Res* 2012; 53: 2038–2045.
10. Vanlandewijck M, He L, Mäe MA, et al. A molecular atlas of cell types and zonation in the brain vasculature. *Nature* 2018; 554: 475–480.
11. Peng X, Carhuapoma JR, Bhardwaj A, et al. Suppression of cortical functional hyperemia to vibrissal stimulation in the rat by epoxigenase inhibitors. *Am J Physiol Heart Circ Physiol* 2002; 283: H2029–2037.
12. Attwell D, Buchan AM, Charpak S, et al. Glial and neuronal control of brain blood flow. *Nature* 2010; 468: 232–243.
13. Nippert AR, Biesecker KR and Newman EA. Mechanisms mediating functional hyperemia in the brain. *Neuroscientist* 2018; 24: 73–83.
14. Alkayed NJ, Birks EK, Narayanan J, et al. Role of P-450 arachidonic acid epoxigenase in the response of cerebral blood flow to glutamate in rats. *Stroke* 1997; 28: 1066–1072.
15. Davis CM, Liu X and Alkayed NJ. Cytochrome P450 eicosanoids in cerebrovascular function and disease. *Pharmacol Ther* 2017; 179: 31–46.
16. Li PL and Campbell WB. Epoxyeicosatrienoic acids activate K⁺ channels in coronary smooth muscle through a guanine nucleotide binding protein. *Circ Res* 1997; 80: 877–884.
17. MacVicar BA and Newman EA. Astrocyte regulation of blood flow in the brain. *Cold Spring Harb Perspect Biol* 2015; 7.
18. Zhang W, Koerner IP, Noppens R, et al. Soluble epoxide hydrolase: a novel therapeutic target in stroke. *J Cereb Blood Flow Metab* 2007; 27: 1931–1940.
19. Shaik JS, Ahmad M, Li W, et al. Soluble epoxide hydrolase inhibitor trans-4-[4-(3-adamantan-1-yl-ureido)-cyclohexyloxy]-benzoic acid is neuroprotective in rat model of ischemic stroke. *Am J Physiol Heart Circ Physiol* 2013; 305: H1605–1613.
20. Zhang W, Otsuka T, Sugo N, et al. Soluble epoxide hydrolase gene deletion is protective against experimental cerebral ischemia. *Stroke* 2008; 39: 2073–2078.
21. Zuloaga KL, Zhang W, Roese NE, et al. Soluble epoxide hydrolase gene deletion improves blood flow and reduces infarct size after cerebral ischemia in reproductively senescent female mice. *Front Pharmacol* 2014; 5: 290.
22. Marowsky A, Haenel K, Bockamp E, et al. Genetic enhancement of microsomal epoxide hydrolase improves metabolic detoxification but impairs cerebral blood flow regulation. *Arch Toxicol* 2016; 90: 3017–3027.
23. Medhora M, Narayanan J and Harder D. Dual regulation of the cerebral microvasculature by epoxyeicosatrienoic acids. *Trends Cardiovasc Med* 2001; 11: 38–42.
24. Medhora M, Daniels J, Munday K, et al. Epoxigenase-driven angiogenesis in human lung microvascular endothelial cells. *Am J Physiol Heart Circ Physiol* 2003; 284: H215–224.
25. Sander AL, Jakob H, Sommer K, et al. Cytochrome P450-derived epoxyeicosatrienoic acids accelerate wound epithelialization and neovascularization in the hairless mouse ear wound model. *Langenbecks Arch Surg* 2011; 396: 1245–1253.
26. Zhang C and Harder DR. Cerebral capillary endothelial cell mitogenesis and morphogenesis induced by astrocytic epoxyeicosatrienoic acid. *Stroke* 2002; 33: 2957–2964.
27. Pozzi A, Macias-Perez I, Abair T, et al. Characterization of 5,6- and 8,9-epoxyeicosatrienoic acids (5,6- and 8,9-EET) as potent in vivo angiogenic lipids. *J Biol Chem* 2005; 280: 27138–27146.
28. Sander AL, Sommer K, Neumayer T, et al. Soluble epoxide hydrolase disruption as therapeutic target for wound healing. *J Surg Res* 2013; 182: 362–367.
29. Sommer K, Jakob H, Badjlan F, et al. 11,12 and 14,15 epoxyeicosatrienoic acid rescue deteriorated wound healing in ischemia. *PLoS One* 2019; 14: e0209158.
30. Sommer K, Jakob H, Reiche C, et al. 11,12 Epoxyeicosatrienoic acid rescues deteriorated wound healing in diabetes. *Int J Mol Sci* 2021; 22: 11664.
31. Miyata M, Kudo G, Lee YH, et al. Targeted disruption of the microsomal epoxide hydrolase gene. Microsomal epoxide hydrolase is required for the carcinogenic activity of 7,12-dimethylbenz[a]anthracene. *J Biol Chem* 1999; 274: 23963–23968.
32. Sinal CJ, Miyata M, Tohkin M, et al. Targeted disruption of soluble epoxide hydrolase reveals a role in blood pressure regulation. *J Biol Chem* 2000; 275: 40504–40510.
33. Percie du Sert N, Hurst V, Ahluwalia A, et al. The ARRIVE guidelines 2.0: updated guidelines for reporting animal research. *J Physiol* 2020; 598: 3793–3801.
34. Mueggler T, Baumann D, Rausch M, et al. Biccuculline-induced brain activation in mice detected by functional magnetic resonance imaging. *Magn Reson Med* 2001; 46: 292–298.
35. Rebling J, Ben-Yehuda Greenwald M, Wietecha M, et al. Long-term imaging of wound angiogenesis with large scale optoacoustic microscopy. *Adv Sci (Weinh)* 2021; 8: 2004226.
36. Zakharov P, Völker AC, Wyss MT, et al. Dynamic laser speckle imaging of cerebral blood flow. *Opt Express* 2009; 17: 13904–13917.
37. Goldim MPS, Della Giustina A and Petronilho F. Using Evans Blue dye to determine blood-brain barrier integrity in rodents. *Curr Protoc Immunol* 2019; 126: e83.

38. Tsai PS, Kaufhold JP, Blinder P, et al. Correlations of neuronal and microvascular densities in murine cortex revealed by direct counting and colocalization of nuclei and vessels. *J Neurosci* 2009; 29: 14553–14570.
39. Zeller K, Vogel J and Kuschinsky W. Postnatal distribution of Glut1 glucose transporter and relative capillary density in blood-brain barrier structures and circumventricular organs during development. *Brain Res Dev Brain Res* 1996; 91: 200–208.
40. Yue F, Cheng Y, Breschi A, et al. A comparative encyclopedia of DNA elements in the mouse genome. *Nature* 2014; 515: 355–364.
41. Hall CN, Reynell C, Gesslein B, et al. Capillary pericytes regulate cerebral blood flow in health and disease. *Nature* 2014; 508: 55–60.
42. Katz S, Gattegno R, Peko L, et al. Diameter-dependent assessment of microvascular leakage following ultrasound-mediated blood-brain barrier opening. *iScience* 2023; 26: 106965.
43. Vanella L, Canestraro M, Lee CR, et al. Soluble epoxide hydrolase null mice exhibit female and male differences in regulation of vascular homeostasis. *Prostaglandins Other Lipid Mediat* 2015; 120: 139–147.
44. Wang H, Lin L, Jiang J, et al. Up-regulation of endothelial nitric-oxide synthase by endothelium-derived hyperpolarizing factor involves mitogen-activated protein kinase and protein kinase C signaling pathways. *J Pharmacol Exp Ther* 2003; 307: 753–764.
45. Panigrahy D, Edin ML, Lee CR, et al. Epoxyeicosanoids stimulate multiorgan metastasis and tumor dormancy escape in mice. *J Clin Invest* 2012; 122: 178–191.
46. Rand AA, Barnych B, Morisseau C, et al. Cyclooxygenase-derived proangiogenic metabolites of epoxyeicosatrienoic acids. *Proc Natl Acad Sci U S A* 2017; 114: 4370–4375.
47. Rand AA, Rajamani A, Kodani SD, et al. Epoxyeicosatrienoic acid (EET)-stimulated angiogenesis is mediated by epoxy hydroxyeicosatrienoic acids (EHETs) formed from COX-2. *J Lipid Res* 2019; 60: 1996–2005.
48. Ribatti D, Nico B and Crivellato E. The role of pericytes in angiogenesis. *Int J Dev Biol* 2011; 55: 261–268.
49. Armulik A, Genové G and Betsholtz C. Pericytes: developmental, physiological, and pathological perspectives, problems, and promises. *Developmental Cell* 2011; 21: 193–215.
50. Spector AA and Norris AW. Action of epoxyeicosatrienoic acids on cellular function. *Am J Physiol Cell Physiol* 2007; 292: C996–1012.
51. Zhang W, Davis CM, Zeppenfeld DM, et al. Role of endothelium-pericyte signaling in capillary blood flow response to neuronal activity. *J Cereb Blood Flow Metab* 2021; 41: 1873–1885.
52. Zhang Y, Hong G, Lee KS, et al. Inhibition of soluble epoxide hydrolase augments astrocyte release of vascular endothelial growth factor and neuronal recovery after oxygen-glucose deprivation. *J Neurochem* 2017; 140: 814–825.
53. Hercule HC, Schunck WH, Gross V, et al. Interaction between P450 eicosanoids and nitric oxide in the control of arterial tone in mice. *Arterioscler Thromb Vasc Biol* 2009; 29: 54–60.
54. Wang S, Qi Y, Yu L, et al. Endogenous nitric oxide regulates blood vessel growth factors, capillaries in the cortex, and memory retention in Sprague-Dawley rats. *Am J Transl Res* 2016; 8: 5271–5285.
55. Wang Y, Wei X, Xiao X, et al. Arachidonic acid epoxide hydrolase metabolites stimulate endothelial cell growth and angiogenesis via mitogen-activated protein kinase and phosphatidylinositol 3-kinase/Akt signaling pathways. *J Pharmacol Exp Ther* 2005; 314: 522–532.
56. Ding Y, Frömel T, Popp R, et al. The biological actions of 11,12-epoxyeicosatrienoic acid in endothelial cells are specific to the R/S-enantiomer and require the G(s) protein. *J Pharmacol Exp Ther* 2014; 350: 14–21.
57. Park SK, Herrnreiter A, Pfister SL, et al. GPR40 is a low-affinity epoxyeicosatrienoic acid receptor in vascular cells. *J Biol Chem* 2018; 293: 10675–10691.
58. Liu X, Qian ZY, Xie F, et al. Functional screening for G protein-coupled receptor targets of 14,15-epoxyeicosatrienoic acid. *Prostaglandins Other Lipid Mediat* 2017; 132: 31–40.
59. Steinman J, Koletar MM, Stefanovic B, et al. 3D morphological analysis of the mouse cerebral vasculature: Comparison of in vivo and ex vivo methods. *PLoS One* 2017; 12: e0186676.
60. Cruz Hernández JC, Bracko O, Kersbergen CJ, et al. Neutrophil adhesion in brain capillaries reduces cortical blood flow and impairs memory function in Alzheimer's disease mouse models. *Nat Neurosci* 2019; 22: 413–420.
61. Tata DA and Anderson BJ. A new method for the investigation of capillary structure. *J Neurosci Methods* 2002; 113: 199–206.
62. Altura BT and Altura BM. Effects of barbiturates, phenylcyclidine, ketamine and analogs on cerebral circulation and cerebrovascular muscle. *Microcirc Endothelium Lymphatics* 1984; 1: 169–184.
63. Zhang W, Iliff JJ, Campbell CJ, et al. Role of soluble epoxide hydrolase in the sex-specific vascular response to cerebral ischemia. *J Cereb Blood Flow Metab* 2009; 29: 1475–1481. 20090527.
64. Morisseau C, Newman JW, Wheelock CE, et al. Development of metabolically stable inhibitors of Mammalian microsomal epoxide hydrolase. *Chem Res Toxicol* 2008; 21: 951–957.
65. Barnych B, Singh N, Negrel S, et al. Development of potent inhibitors of the human microsomal epoxide hydrolase. *Eur J Med Chem* 2020; 193: 112206.